J Adv Ceram

Research Article

Multiscale particle grading of monodisperse spherical Al_2O_3 ceramics: Sintering activation energy and densification mechanisms

Mingda Huo, Haoyang Qu, Jingyi Zhang, Ruohan Li, Jinze Du, Tianyu Zhu, Yaxuan Li, Weiguo Cheng, Xiaohong Sun✉

Cite this article: Huo M, Qu H, Zhang J, et al. *J Adv Ceram* 2026, **15**(6): 9221311. https://doi.org/10.26599/JAC.2026.9221311

ABSTRACT: To address the limitations of existing research on ceramic particle grading regarding powder agglomeration and mechanistic depth, this study employed four types of uniform, monodisperse spherical α-Al_2O_3 powders. A series of grading systems, ranging from binary to quaternary, were constructed to systematically investigate the influence of multiscale particle grading on the microstructure, sintering kinetics, and mechanical properties of the ceramics. Through multiscale characterization spanning from nano- to microscale and from two to three dimensions, it was confirmed that the quaternary grading system (PG5) exhibited the fastest densification rate, the lowest porosity, and superior mechanical properties. Based on thermomechanical analysis (TMA) combined with Arrhenius equation calculations, the PG5 sample possessed the lowest sintering activation energy (129.95 kJ/mol). The results of the Rietveld refinement also showed the same trend. This revealed the essence of its rapid densification from the perspectives of geometric packing, atomic-level sintering shrinkage, and sintering kinetics. Specifically, multiscale grading not only optimized the particle contact network and mass transport pathways but, more crucially, significantly reduced the energy barrier for atomic migration, thereby fundamentally accelerating and completing the densification process. This study provides a clear mechanistic understanding and experimental basis for tailoring ceramic microstructures and sintering kinetics through rational powder structural design.

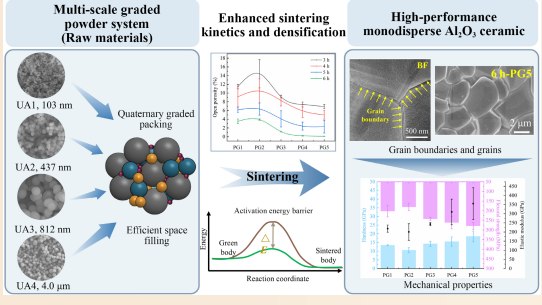

KEYWORDS: Al_2O_3 ceramics; multiscale particle grading; monodisperse powders; sintering activation energy

1 Introduction

Due to their exceptional high-temperature stability, superior mechanical strength, and outstanding chemical inertness, Al_2O_3 ceramics have become indispensable key materials in modern industry and cutting-edge technology [1–4]. Ranging from wear-resistant components in precision machinery and refractory linings in high-temperature furnaces to substrates in semiconductor manufacturing and artificial joint implants in biomedicine, their applications profoundly impact the development of the energy, information, medical, and high-end equipment manufacturing sectors [5–9]. These extensive and demanding application scenarios invariably impose stringent requirements on the microstructural integrity and performance reliability of Al_2O_3 ceramics. The core processing step to achieve these goals lies in sintering [10–12]. However, the initial characteristics of the raw powder and its packing configuration in the green body fundamentally predetermine the pathways and efficiency of mass transport during sintering, thereby dictating the kinetics of pore elimination and the morphology of the final grain boundary network [13–15]. The use of powders with a single particle size distribution often faces a dilemma where the packing density and sintering activity cannot be simultaneously optimized. Fine powders possess a high sintering driving force but are prone to agglomeration, whereas coarse powders exhibit a weak sintering driving force and are susceptible to grain coarsening. This often leads to defects during the forming process or induces abnormal grain growth during sintering, resulting in isolated residual pores at grain boundaries that severely deteriorate the mechanical properties and reliability of the material [16,17]. Therefore, determining how to construct an initial structure conducive to efficient and uniform densification through the rational design of powder systems remains a key scientific issue for breaking through the performance bottlenecks of Al_2O_3 ceramics and expanding their applications.

To resolve the aforementioned dilemma, the introduction of

School of Materials Science and Engineering, State Key Laboratory of Precious Metal Functional Materials, Key Laboratory of Advanced Ceramics and Machining Technology of Ministry of Education, Tianjin University, Tianjin 300072, China.

✉ Corresponding author. E-mail: sunxh@tju.edu.cn

Received: February 3, 2026; Revised: April 28, 2026; Accepted: May 2, 2026

multiscale particle grading to optimize the powder packing configuration is regarded as a highly promising solution. In practical industrial applications and engineering manufacturing, particle composition optimization has already been widely employed as a highly effective and routine strategy to maximize solid loading, improve green body density, and ultimately enhance the mechanical performance of ceramics. Numerous studies have confirmed that filling the interstices between coarse particles with fine particles of appropriate sizes can significantly improve the packing density of the green body and reduce the initial pore size, thereby achieving a faster shrinkage rate during the initial stage of sintering [18–25]. However, current research and practical implementations in this field are constrained by two notable limitations that hinder the development of a universal and profound understanding of the grading effect. First, regarding the construction of model systems, most studies and industrial practices utilize commercial powders that typically exhibit broad particle size distributions, irregular morphologies, and unavoidable agglomeration. This makes it difficult for researchers to attribute observed phenomena solely and clearly to the influence of particle size distribution as the core variable [15,21,25–27]. Consequently, conventional grading optimizations often rely heavily on macroscopic empirical trial-and-error rather than precise theoretical guidance. In other words, the lack of research using strictly monodisperse, highly spherical powders as building blocks prevents us from revealing the intrinsic effects of grading theory at an ideal experimental level. Second, and more critically, regarding the depth of mechanistic elucidation, existing studies predominantly attribute performance improvements to the physical factor of increased initial packing density. While this is undoubtedly important, sintering is a nonequilibrium process governed jointly by thermodynamic driving forces and kinetic rates [28–31]. Relying solely on packing density fails to explain why different grading systems with similar green densities exhibit distinctly different densification rates and final microstructures during sintering, nor can it clarify the essence of this phenomenon. The fundamental reason is that the research perspective is largely confined to comparing macroscopic parameters such as density and porosity, without delving into the intrinsic kinetic parameters that dictate the sintering process, specifically the evolution of sintering activation energy. Activation energy is a direct measure of the difficulty of atomic or vacancy diffusion [27,28,32]. Particle grading alters not only the porosity but also the fundamental nature of the sintering process itself, which inevitably induces dynamic changes in activation energy. Neglecting to track and analyze this core kinetic parameter makes it difficult to fundamentally reveal the specific mechanisms by which multiscale grading regulates sintering behavior, thereby leaving research conclusions at the level of empirical correlation and lacking universal mechanistic support.

To address the aforementioned research gaps, this study employed four types of uniform, monodisperse spherical α-Al_2O_3 powders as ideal building blocks to construct multiscale particle grading systems. Based on this foundation, five grading formulations ranging from binary and ternary to quaternary systems were precisely designed. This approach allowed for a focused investigation into the effects of particle size distribution while maximally excluding confounding factors such as particle morphology and agglomeration. First, the differences in open porosity over time at constant temperature, microstructural evolution, and mechanical properties of the different grading systems were systematically characterized to establish the superiority of quaternary grading (PG5). Furthermore, the core innovation of this study lies in the use of shrinkage curves precisely recorded by thermomechanical analysis (TMA), combined with the Arrhenius equation, to quantitatively calculate and compare the sintering activation energy and its dynamic evolution. This revealed the mechanisms by which multiscale particle grading governs the sintering kinetics of α-Al_2O_3 ceramics. Multiscale grading constructed a more efficient short-range mass transport network during the sintering process, manifesting as a lower sintering activation energy. This study provided multiscale evidence—spanning from micron to nano and from 2D to 3D—demonstrating that the quaternary grading achieved more complete densification with fewer defects, offering direct structural evidence for its performance advantages. Additionally, the study elucidated the kinetic origins of the densification retardation phenomenon observed between different particle grading systems, thereby providing theoretical support for the rational design of powders for high-performance ceramics.

2 Experimental

2.1 Raw materials and ceramic forming and sintering

The α-Al_2O_3 powders used in this experiment were synthesized in-house via a hydrothermal method, and detailed preparation procedures can be found in previous work [33–36]. The four powders, with distinct particle sizes, exhibited not only excellent dispersibility but also a uniform, spherical morphology. They were designated UA1 through UA4 (where U denotes Uniform and A denotes α-Al_2O_3). To accurately investigate the intrinsic sintering potential and green body packing characteristics of the different graded powders, no sintering additives were introduced throughout the experiment. For preparation, the powders were batched according to the five grading formulations (PG, where P denotes particle, and G denotes gradation) listed in Table 1. The mass fractions for the grading formulations were systematically designed based on the principles of the classic Horsfield discrete particle packing model. The Horsfield model—which describes the optimal filling of interstitial voids within a primary coarse sphere skeleton using successively smaller secondary, tertiary, and quaternary spheres—provided an ideal theoretical framework. The mixtures were ball-milled in anhydrous ethanol at a speed of 400 r/min for 24 h to ensure compositional homogeneity. Specifically, ZrO_2 grinding balls with diameters of 10 and 6 mm were utilized at a mass ratio of 1 : 1. The mass ratio of the dispersion medium (anhydrous ethanol), grinding balls, and Al_2O_3 powder was strictly controlled at 3 : 2 : 1 to achieve optimal mixing efficiency without altering the original spherical morphology of the monodisperse powders. After drying, the mixed powders were formed into structurally reliable green bodies via uniaxial dry pressing at 50 MPa followed by cold isostatic pressing at 200 MPa. Subsequently, the green bodies were placed in a muffle furnace and heated to 1600 °C at a rate of 1 °C/min, where they were held for 3, 4, 5, and 6 h to achieve densification.

Table 1 Proportion of different types of powders in particle gradation (Unit: wt%)

Formulation	UA1	UA2	UA3	UA4
PG1	—	25	—	75
PG2	—	—	30	70
PG3	—	15	25	60
PG4	15	—	20	65
PG5	10	15	20	55

2.2 Characterizations

To comprehensively analyze the material characteristics, this study established a multidimensional characterization framework spanning from basic powder physical properties to the macroscopic and microscopic structures of the ceramics. First, depending on the particle size range, dynamic light scattering (DLS) and a laser particle size analyzer were employed to determine the particle size distributions of powders smaller than and larger than 3 μm, respectively, to assess their agglomeration states. Phase compositions were identified using X-ray diffraction (XRD) with a scanning range of 10°–90°. Rietveld refinement was performed using the pseudo-Voigt peak shape profile in TOPAS software. The microscopic morphologies of the powders and the ceramic samples were observed using cold field emission scanning electron microscopy (FE–SEM); the ceramic samples were thermally etched at 1500 °C for 30 min prior to observation. The bulk density and open porosity of the ceramics were determined using the Archimedes method. For green bodies, to avoid liquid infiltration and structural collapse during immersion, the initial green density was calculated using the precise geometric method by measuring the mass and physical dimensions of the pressed pellets. The elastic modulus and hardness were evaluated via a nanoindentation tester (maximum load: 1000 μN; holding time per stage: 10 s), while the room-temperature flexural strength was measured using the three-point bending method. To properly evaluate data reproducibility and reliability, at least 5 specimens were tested for each grading formulation. The mechanical property results are reported as the mean value. Furthermore, for sintering kinetics analysis, the thermal expansion behavior of the ceramic green bodies was tested using a thermomechanical analyzer in an air atmosphere from 30 to 1550 °C at a heating rate of 18 °C/min. The resulting expansion curves were utilized to calculate the sintering activation energy of different formulations based on the Arrhenius equation. It is worth noting that although the heating rate differed from that used during ceramic sintering, the method for calculating activation energy via the Arrhenius equation remains valid, as the heating rate (18 °C/min) was quantitatively incorporated into the calculation (see Eq. (4)). For the PG5 sample sintered at 1600 °C for 6 h, a focused ion beam (FIB) system was further employed to prepare specimens for transmission electron microscopy (TEM) to analyze grain boundary characteristics. Additionally, an X-ray 3D microscopy (Micro–CT) system with a spatial resolution of 0.5 μm combined with Dragonfly software was used for 3D reconstruction to clearly characterize the internal pore structure in three dimensions.

3 Results and discussion

3.1 Microstructural and morphological analysis of monodisperse spherical α-Al_2O_3 powder

The excellent dispersibility and particle size uniformity of the α-Al_2O_3 powders provided a critical material foundation for the subsequent preparation of particle graded ceramics. As shown in Figs. 1(a)–1(d), the four powders, designated UA1–UA4, all exhibited a regular spherical morphology under SEM. The particles were well separated with no apparent agglomeration, visually demonstrating their highly dispersed nature. Further verification through particle size analysis, as presented in Figs. 1(e)–1(h), revealed that the particle size distribution curve for each powder exhibited a monomodal distribution, which directly confirmed the monodisperse nature and uniformity of the powders. Specifically, the measured average particle sizes for UA1 through UA4 were 103 nm, 437 nm, 812 nm, and 4 μm, respectively. These quantitative data were consistent with the morphological observations, collectively indicating that the utilized powders possessed the ideal physical properties of uniform particle size and monodispersity.

The impurity content is one of the critical factors influencing the properties and sintering kinetics of α-Al_2O_3 ceramics. To evaluate the purity of the raw materials used in this study, XRD analysis was performed on the four monodisperse spherical α-Al_2O_3 powders (UA1–UA4). As shown in Fig. 2, the diffraction patterns of all samples exhibited sharp and consistent diffraction peaks, indicating a high degree of crystallinity. Although slight fluctuations existed in the relative intensities of the diffraction peaks among powders of different particle sizes, the positions of all peaks corresponded perfectly with the standard diffraction data for α-Al_2O_3, and no spurious peaks originating from other crystalline phases were observed within the detection range. These results fully demonstrated that the powders synthesized via the hydrothermal method possessed high phase purity, with no detectable impurity phases introduced. Furthermore, the rigorous washing and high-temperature calcination processes during powder synthesis completely volatilized and removed residual elements such as S from the precursors. Because the entire synthesis route strictly excluded sources of Na, Mg, Ca, and K (impurities notorious for segregating at grain boundaries and inducing liquid-phase assisted sintering), this fundamental purity effectively ruled out the interference of impurity-induced diffusion

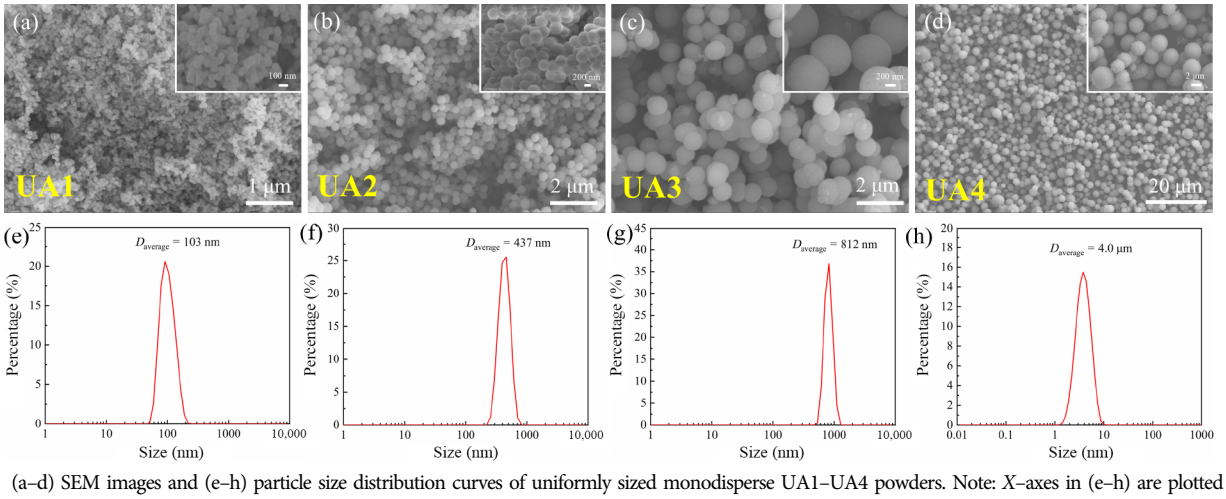

Fig. 1 (a–d) SEM images and (e–h) particle size distribution curves of uniformly sized monodisperse UA1–UA4 powders. Note: *X*–axes in (e–h) are plotted on a logarithmic scale.

pathways in the subsequent analysis. Therefore, combined with the previously observed spherical morphology and monodisperse characteristics, it was confirmed that the utilized powders exhibited high consistency in terms of crystal structure, chemical purity, and physical morphology. This provided a pure and homogeneous material foundation for the subsequent investigation into the intrinsic sintering behavior and properties of the graded ceramics.

3.2 Regulatory role of particle gradation on ceramic microstructure and mechanical properties

The initial geometric packing efficiency of the green bodies served as the essential thermodynamic foundation for the subsequent sintering behavior. Consistent with the theoretical expectations of the Horsfield packing model, the geometric green density measurements revealed a clear correlation between the complexity of the gradation and the initial packing efficiency. The measured experimental green densities for PG1 through PG5 were 2.05, 2.01, 2.10, 2.11, and 2.15 g/cm^3, respectively. The results clearly indicated that PG2 exhibited the lowest density among all formulations. This confirmed that the bimodal packing of coarse particles without the interstitial filling of nanoparticles resulted in a relatively loose initial structure, which was predicted to significantly elongate the effective atomic diffusion distances during the subsequent sintering process. The quaternary formulation PG5 exhibited the highest green density, significantly outperforming the binary formulations. This quantitative experimental evidence confirmed that hierarchical interstitial filling by monodisperse fine particles successfully translated theoretical geometric packing advantages into actual macroscopic densification at the green stage. Figure 3 shows the evolution of the open porosity and bulk density for five ceramic samples with different particle size grades (PG1–PG5) after holding at 1600 °C for varying times. From the perspective of sintering time, the densification degree of all formulations improved with prolonged holding time; porosity gradually decreased while bulk density correspondingly increased, adhering to the general laws of sintering densification. This was attributed to the fact that extended holding time provided sufficient thermodynamic and kinetic conditions for atomic diffusion and grain boundary migration, thereby promoting pore elimination and closure [37]. However, significant differences were observed in the densification rates among the different grading systems. PG4 and PG5 exhibited a steeper downward trend in porosity, indicating that multicomponent grading systems possessed a higher sintering driving force during sintering. Comparing the grading formulation dimensions, the quaternary grading system (PG5) demonstrated the most superior sintering performance, followed by the ternary systems (PG3 and PG4), while the binary systems (PG1 and PG2) were relatively inferior. For a given formulation across different sintering times, it was evident that prolonging the sintering time promoted densification for all samples; however, the magnitude of improvement varied by formulation. Regarding open porosity, PG5 maintained the lowest values at all tested time points, as shown in Fig. 3(a). At the initial stage of holding at 1600 °C for 3 h, the porosity of PG5 had already dropped to 6.9%, which was significantly lower than the 14.4% of the binary grading PG2 and the 11.5% of PG1. As sintering progressed to 6 h, PG5 achieved near-full densification with a porosity of only 0.1%. In comparison, PG4 decreased to 0.2%, while PG3, PG1, and PG2 decreased to 1.2%, 3.5%, and 3.9%, respectively. The final open porosity of PG4 and PG5, which incorporated UA1 powders, was significantly lower than that of PG1–PG3 without nanopowders. This indicated that the introduction of nanoparticles effectively filled the microvoids formed by the packing of micron-sized particles [38]. Furthermore, the quaternary continuous grading further optimized the space-filling efficiency, resulting in faster densification kinetics. In contrast, the densification rates of the binary gradings PG1 and PG2 were notably slower. Notably, the porosity of PG5 decreased to 2.3% after 5 h of sintering, whereas the binary gradings remained above 3.5% even after 6 h, further highlighting the significant advantage of multiscale grading in promoting sintering. Regarding bulk density, the data presented a trend that corroborated the porosity results, as shown in Fig. 3(b). As the complexity of the grading increased, the final density of the

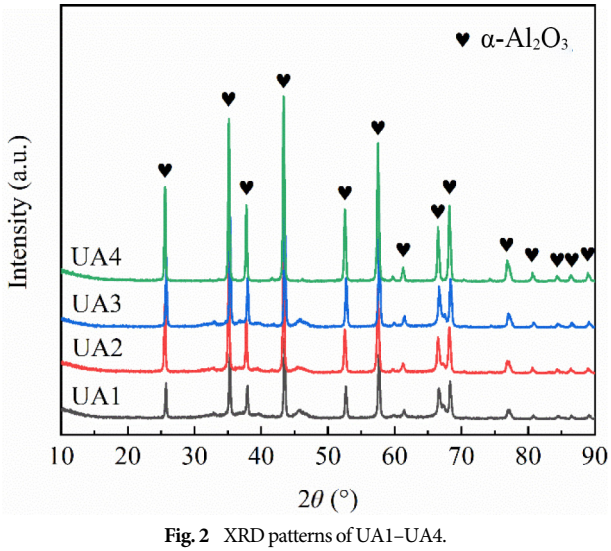

Fig. 2 XRD patterns of UA1–UA4.

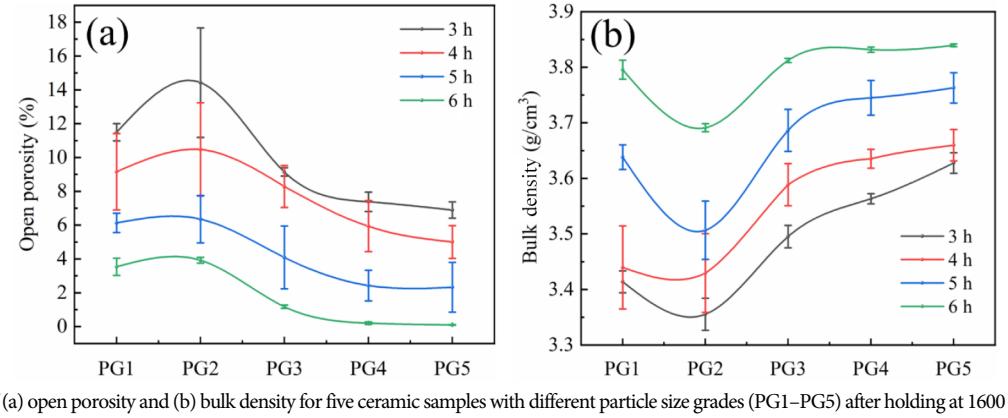

Fig. 3 Evolution of (a) open porosity and (b) bulk density for five ceramic samples with different particle size grades (PG1–PG5) after holding at 1600 °C for varying times.

samples showed a stepwise increase. After holding at 1600 °C for 6 h, the bulk density of PG5 reached a maximum of 3.84 g/cm³. These results indicated that multiscale particle grading design, particularly the rational introduction of nano- and submicron particles, could significantly accelerate the sintering process of Al_2O_3 ceramics. PG5 achieved the optimal macroscopic particle packing density through the quaternary synergistic grading of 103 nm, 437 nm, 812 nm, and 4.0 μm powders. This multiscale grading strategy not only improved the initial packing efficiency at the green body stage but also significantly accelerated the densification process during high-temperature sintering. This was achieved through the geometric effect of "small particles filling the interstices of large particles" and the high surface energy driving effect of nanoparticles, effectively inhibiting the formation of residual pores. The ultimate densification was synergistically governed by both the number of particle grading levels and the precise particle size ratio. The number of grading levels established the theoretical limit of hierarchical void filling, whereas an appropriate particle size ratio guaranteed that finer particles could seamlessly occupy the interstitial voids of the primary skeleton without inducing a wedging effect that expanded the preexisting pores.

Figure 4 shows thermally etched SEM images of five ceramic samples with different particle size grades (PG1–PG5) held at 1600 °C for varying durations, clearly revealing the evolution of their microstructures. From a temporal perspective, all sample groups exhibited a distinct trend toward densification as the sintering time increased. During the 3 and 4 h stage, interparticle sintering necks grew continuously, while irregular micron-scale pores gradually shrank and closed, as shown in Figs. 4(a)–4(j). For instance, the macroscopic bulk density of the optimal PG5 sample increased from 3.63 g/cm³ at 3 h to 3.66 g/cm³ at 4 h. In the 5 and 6 h stages, grain boundaries became well developed, displaying typical polyhedral grain morphologies alongside a significant reduction in porosity, as shown in Figs. 4(k)–4(t), with the density of PG5 further reaching 3.76 g/cm³ at 5 h and peaking at 3.84 g/cm³ after 6 h. From the perspective of grading formulation, the complexity of the particle size gradings directly determined both the rate and final quality of densification. Small amounts of intergranular pores remained visible in the binary grading groups (PG1 and PG2) even after sintering for 6 h. Conversely, the ternary (PG4) and quaternary (PG5) grading groups, which incorporated the fine-grained UA1 component, exhibited higher sintering activity and lacked obvious pore structures. Furthermore, the densification process of the quaternary PG5 sample was notably superior to that of the other formulations, as shown in Figs. 4(e), 4(j), 4(o), and 4(t). At identical sintering times, PG5 exhibited the smallest pore size and the most uniform distribution. Notably, when the sintering time reached 6 h, the PG5 sample displayed a dense grain arrangement with straight grain boundaries and almost no residual pores at triple junctions, presenting a near-ideal dense structure, as shown in Fig. 4(t). To quantitatively evaluate the microstructural evolution and address the concern of whether mixing multiscale powders deteriorated grain size uniformity, a comprehensive statistical analysis of the grain size distribution was performed using the equivalent circle diameter method based on SEM images, as shown in Fig. 5. The histograms explicitly demonstrated that the multiscale graded ceramics (particularly the optimal PG5) did not suffer from microstructural degradation. Instead, they maintained a highly concentrated, mono-modal normal distribution throughout the sintering process. For instance, after sintering at 1600 °C for 6 h, despite the initial massive size discrepancy between UA1 and UA4, the final grain size of PG5 was narrowly distributed around an average of (4.0±1.5) μm, with an absolute absence of abnormal grain growth, as shown in Fig. 5(t). This exceptional uniformity fundamentally stemmed from the ideal monodispersity of raw powders. The uniformly dispersed nanoparticles locally accelerated densification in the interstices and subsequently formed a homogeneous boundary network that effectively pinned localized abnormal migration, successfully breaking the traditional limitation that broad particle size distributions inevitably lead to inhomogeneous microstructures.

To gain in-depth insights into the densification mechanism of

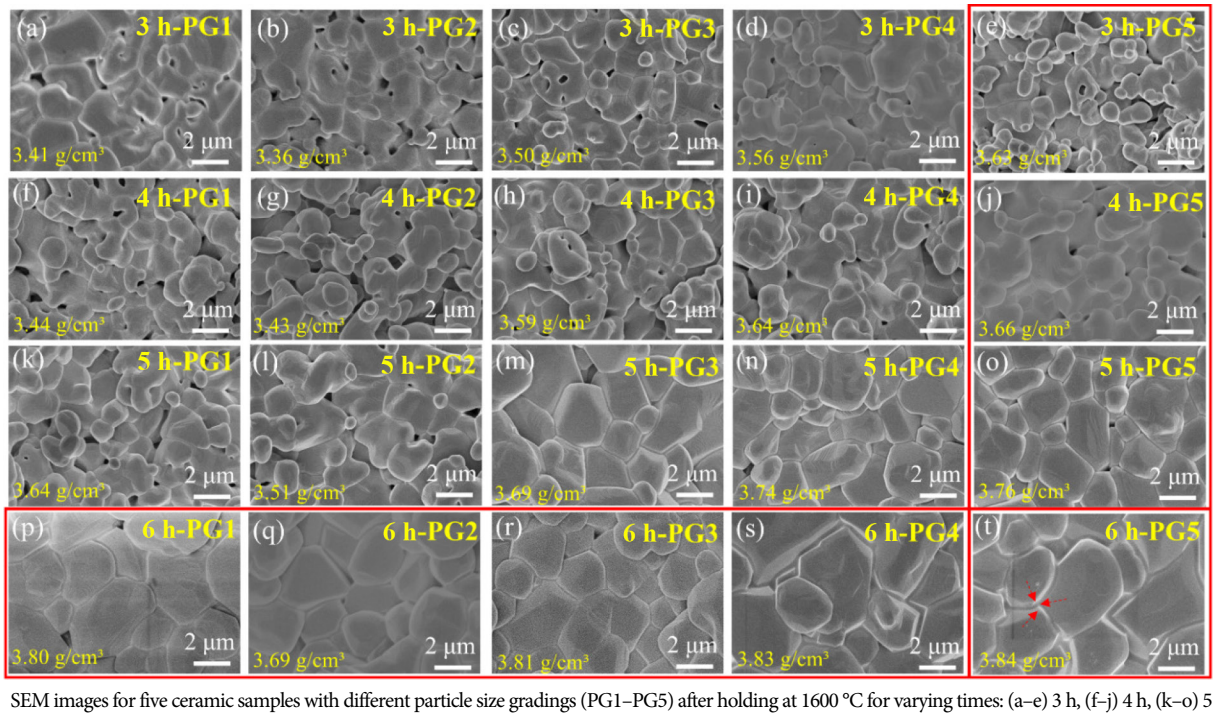

Fig. 4 SEM images for five ceramic samples with different particle size gradings (PG1–PG5) after holding at 1600 °C for varying times: (a–e) 3 h, (f–j) 4 h, (k–o) 5 h, and (p–t) 6 h. The corresponding bulk density values (g/cm³) are annotated in each subimage to quantitatively correlate the microstructural evolution with densification.

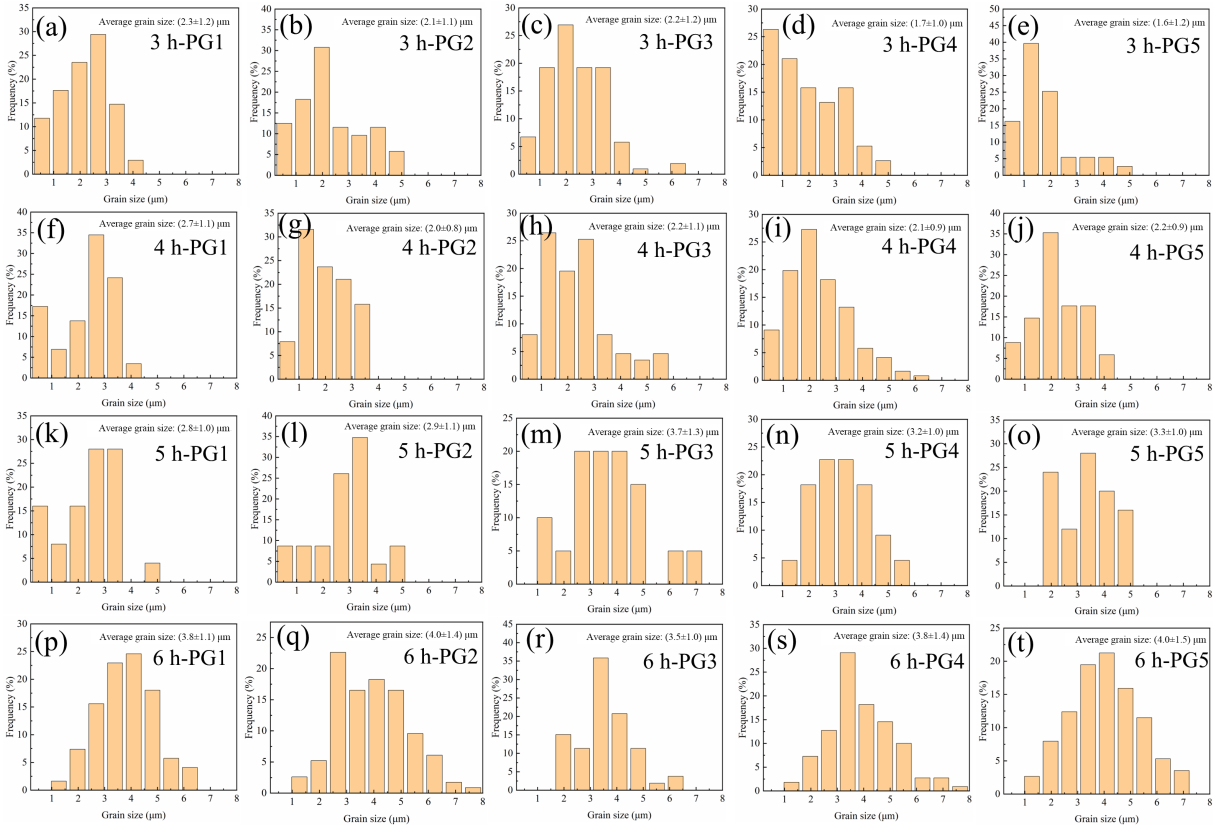

Fig. 5 Particle size distribution curve for five ceramic samples with different particle size grades (PG1–PG5) after holding at 1600 °C for varying time: (a–e) 3 h, (f–j) 4 h, (k–o) 5 h, and (p–t) 6 h.

the quaternary particle grading ceramic (PG5) at the nanoscale after holding at 1600 °C for 6 h, site-specific TEM specimens were prepared using the FIB technique for multiscale microstructural characterization, as shown in Fig. 6. Figures 6(a) and 6(b) show the FIB sampling location and the macroscopic morphology of the prepared lamella, respectively. The observations reveal a highly homogeneous and dense internal structure, with no detectable microcracks or residual pores at the micron scale. This provides direct evidence of the excellent pore-filling capability of the quaternary particle grading strategy. Further high-magnification HAABF–STEM imaging of the grain boundary regions demonstrated extremely intimate intergranular bonding and straight grain boundaries, with an absence of nanoscale porosity, indicating that sintering effectively promoted pore elimination, as shown in Fig. 6(c). The high–resolution transmission electron microscopy (HRTEM) image of the grain boundary in Fig. 6(d), along with the corresponding lattice fringe pattern, clearly reveals the atomic arrangement at the grain interface. The lattice fringes were clear, continuous, and ordered, indicating high crystallinity. The grains were tightly interlocked at the boundary, corresponding to the (110) plane of α-Al_2O_3, as shown in Fig. 6(e). Furthermore, the measured intergranular spacing was approximately 3 nm (determined using DigitalMicrograph software), quantitatively confirming the tight bonding between grains, as shown in Fig. 6(f). As depicted in the dark field (DF) image (Fig. 6(g)) and the corresponding energy dispersive spectroscopy (EDS) elemental maps (Figs. 6(h) and 6(i)), both Al and O were homogeneously distributed across the grains and the boundary without any localized enrichment or depletion. Crucially, the precise point EDS spectrum collected strictly at the grain boundary (Fig. 6(j)) exclusively displayed peaks for Al, O, and Cu (signal from the TEM copper grid). The complete absence of typical trace impurities definitively ruled out the existence of amorphous intergranular films or liquid-phase assisted sintering. These intrinsic chemical and microstructural pieces of evidence collectively and profoundly confirmed that the markedly lowered activation energy and accelerated densification kinetics in the PG5 sample were purely driven by the optimized solid-state mass transport pathways established by the multiscale geometric grading, rather than being an artifact of impurity segregation. This FIB–TEM microstructural evidence corroborated the SEM results discussed earlier, providing strong nanoscale support for the low porosity (0.1%) of the PG5 sample.

To comprehensively evaluate the macroscopic structure of the PG5 sample sintered at 1600 °C for 6 h and to corroborate its low porosity, Micro–CT and three-dimensional visualization analysis were performed, as shown in Fig. 7. Figure 7(a) shows the complete 3D model of the PG5 ceramic sample, displaying the overall morphology of the sintered ceramic. Figures 7(b) and 7(d) show 2D CT cross–sectional images along the *Z*– and *Y*–axes, respectively, while Figs. 7(c) and 7(e) show the corresponding CT reconstructed images processed using Dragonfly software. A comparison of the multidimensional slices and reconstructed images revealed that the sample interior exhibited a highly homogeneous and dense structure. No obvious macrocracks or large-scale pore defects (above the submicron detection limit of the Micro–CT resolution) were observed in the cross–sections along the *Z*– and *Y*–axes, nor was an interconnected pore network formed. While Micro–CT provides valuable macroscopic validation of structural integrity, the absence of submicron and nanoscale pores was further definitively confirmed by the aforementioned high–resolution FIB–TEM analysis. These macroscopic nondestructive testing results were highly consistent with the microstructural grain boundary densification confirmed

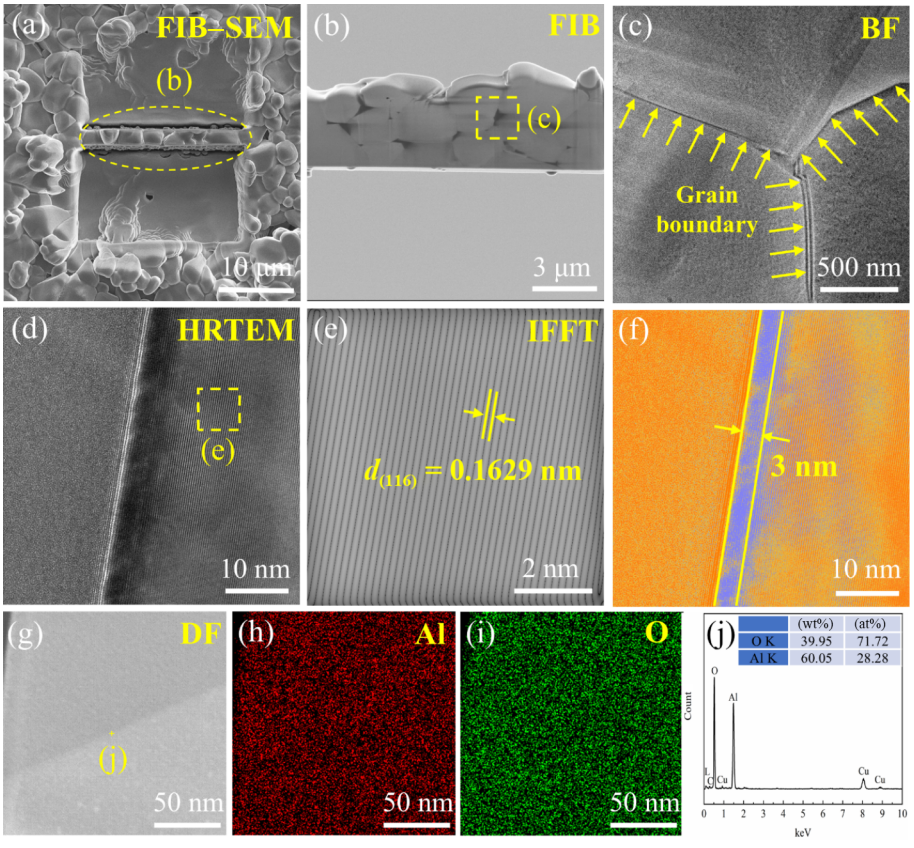

Fig. 6 FIB–SEM, HAABF, HRTEM, and IFFT of the quaternary graded sample (PG5) after sintering at 1600 °C for 6 h: (a) sampling location, (b) macroscopic morphology after FIB, (c) HAABF image corresponding to the yellow line section in (b), (d) HRTEM image, (e) IFFT image corresponding to the yellow line section in (d), (f) colorized image at grain boundaries generated using commercial software GMS 3 based on the grayscale values from the HRTEM image in (d), (g) DF image of the grain boundary, (h) EDS result of Al, (i) EDS result of O, and (j) EDS result marked by the yellow cross in (g).

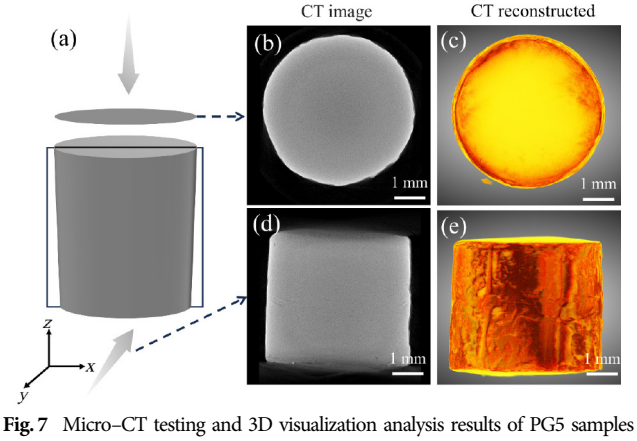

Fig. 7 Micro–CT testing and 3D visualization analysis results of PG5 samples after sintering at 1600 °C for 6 h: (a) 3D model, (b) 2D CT slice image parallel to the *Z*–axis, (c, e) CT reconstructed images processed using Dragonfly software, and (d) 2D CT slice image parallel to the *Y*–axis direction.

by the aforementioned FIB analysis. From a 3D perspective, this intuitively demonstrated that the grading powder (PG5), under optimized sintering conditions, effectively eliminated residual voids from particle packing and the densification process. Consequently, a ceramic matrix free of obvious defects at both macro- and microscales were formed.

Figure 8 shows the hardness, flexural strength, and elastic modulus of the five formulations (PG1–PG5) after sintering at 1600 °C for 6 h. The mechanical properties exhibited a significant trend that aligned with the variations in bulk density. The quaternary particle grading PG5 sample exhibited superior comprehensive properties, achieving peak hardness, flexural strength, and elastic modulus values of 18.5 GPa, 278.9 MPa, and 355.5 GPa, respectively. The ternary grading groups (PG3 and PG4) followed, with PG4 (containing UA1 particles) outperforming PG3 across all metrics. In contrast, the binary grading PG2 sample displayed the lowest performance, with values of only 10.6 GPa, 180.5 MPa, and 200.2 GPa. This trend clearly confirmed that as the number of grading components increased and fine particles were rationally introduced, the resulting reduction in porosity directly led to a simultaneous enhancement in hardness, flexural strength, and elastic modulus. The excellent mechanical properties of PG5 corresponded to its near-pore-free dense microstructure previously revealed by SEM, FIB, and Micro-CT analyses. This demonstrated that multiscale grading, by promoting sintering densification, was an effective strategy for achieving structural reinforcement and performance enhancement in Al_2O_3 ceramics.

Figure 9 shows the load-displacement curves of the PG1–PG5 samples sintered at 1600 °C for 6 h. These curves not only directly reflect the material's deformation behavior at the microscopic scale but also reveal the underlying mechanism regarding the effect of micropore structure on mechanical properties. It could be clearly observed that under constant load conditions, the indentation depths of the samples with different grades differed significantly, following a decreasing order of PG2 > PG1 > PG3 > PG4 > PG5. Specifically, the binary grading PG2 sample exhibited the largest indentation depth, indicating the weakest resistance to plastic deformation. Conversely, the quaternary particle grading PG5 sample showed the smallest peak displacement with minimal indentation depth, directly corroborating its highest Vickers

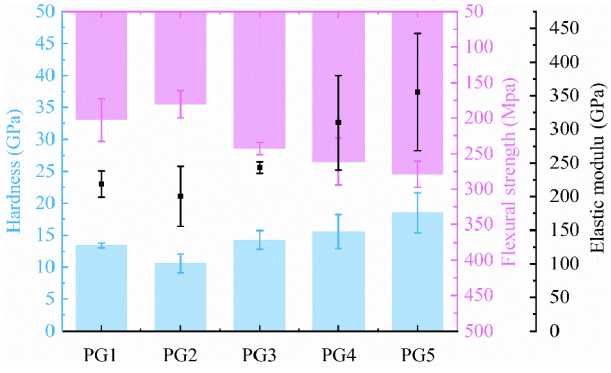

Fig. 8 Hardness, flexural strength, and elastic modulus of five graded ceramics after sintering at 1600 °C for 6 h.

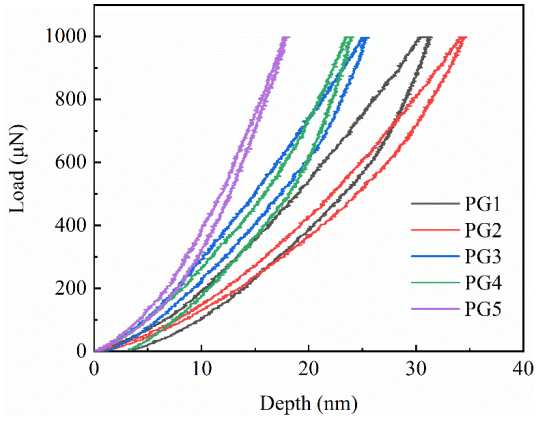

Fig. 9 Load–displacement curves of five graded ceramics after sintering at 1600 °C for 6 h.

hardness value of 18.5 GPa. Furthermore, the slope of the unloading curve indicated that the unloading stiffness of PG5 was significantly higher than that of the other compositions, corresponding to its highest elastic modulus. The fundamental reason for this difference lies in the weakening effect of porosity on the material's deformation resistance [39,40]. For samples such as binary PG2, pores are prone to collapse or induce incompatible sliding of surrounding grains during loading, resulting in a larger macroscopic indentation depth and lower hardness. In contrast, benefiting from the dense packing facilitated by the quaternary particle grading strategy, the PG5 sample possessed a highly dense microstructure. During indentation, the indenter interacted directly with a continuous and strongly bonded Al_2O_3 crystalline matrix. Consequently, PG5 not only exhibited the smallest displacement but also displayed a significantly steeper unloading slope compared to the other compositions, resulting in the highest hardness and elastic modulus. It should be noted that while PG5 exhibited the best comprehensive performance among the tested groups, its absolute mechanical values were not yet at the state-of-the-art level for advanced Al_2O_3 ceramics. This was primarily because the current study intentionally employed highly pure, additive-free powders and conventional pressureless sintering to strictly isolate and investigate the intrinsic physical effects of multiscale grading on sintering kinetics. Without the use of grain growth inhibitors or advanced consolidation pressures, the absolute mechanical limits were naturally constrained. Nevertheless, the significant relative enhancement achieved by PG5 validated the effectiveness of the grading design. Based on this fundamental framework, future research directions would focus on combining this optimal multiscale geometric grading strategy with chemical doping modifications and advanced sintering technologies (such as SPS or two-step sintering) to further suppress grain growth and push the absolute mechanical properties to top-tier levels.

3.3 Evolution of sintering activation energy and mechanism of densification delay

Why does PG5 (quaternary particle grading) achieve faster densification and a lower final porosity? What are the fundamental differences compared to other samples? To address these questions, it is necessary to deeply analyze the dynamic sintering behavior of multiscale graded powders during the heating process. Figure 10 shows the variations in the thermal expansion coefficient ($d\varepsilon/dT$) and strain ($\Delta L/L_0$) as a function of temperature for samples PG1–PG5 (Figs. 10(a)–10(e)), as well as the densification rate, defined as the first derivative of shrinkage strain with respect to time [41], as shown in Fig. 10(f), where ΔL is the change in length, L_0 is the initial length, T is the temperature, and ε and $\Delta L/L_0$ are the strain, respectively.

As shown in Figs. 10(a)–10(e), all samples exhibited similar positive thermal expansion behavior in the low-temperature region. As the temperature rose to the initial stage of sintering, interparticle contact necks began to form and grow [42–44]. Consequently, the sintering shrinkage mechanism gradually dominated, causing the apparent thermal expansion coefficient to drop sharply and transition to negative values, marking the onset of the densification process [45]. Comparing the strain curves of PG1–PG5, the PG5 sample with graded quaternary particles exhibited a significant shrinkage trend at a relatively lower temperature (1294 °C). Its strain curve displayed the steepest slope, indicating the most rapid densification process, with a maximum linear shrinkage of 3.53%. In contrast, the onset temperatures of shrinkage for the ternary particle grading groups (PG3 and PG4) were slightly higher at 1320 and 1341 °C, with maximum linear shrinkages of 2.70% and 2.61%, respectively. The binary particle grading groups (PG1 and PG2) exhibited the highest onset temperatures of 1383 and 1400 °C, with maximum linear shrinkages of 1.95% and 1.89%, respectively. This sequence clearly demonstrated a distinct phenomenon of delayed densification. Further observation of the densification rate curves in Fig. 10(f) revealed that PG5 exhibited the highest shrinkage rate, implying that it could rapidly complete the majority of pore elimination and densification. This rapid kinetic response was attributed to the efficient packing structure constructed by quaternary particle grading. Its multilevel particle filling mode significantly increased the number of interparticle contact points and shortened the mass diffusion paths, thereby providing a greater driving force for sintering. Conversely, the lower and broader rate peaks of PG1 and PG2 confirmed their insufficient sintering kinetics, making it difficult for some pores to be effectively expelled within a limited time. This corroborated the porosity observations discussed earlier. The aforementioned TMA data not only quantify the differences in sintering behavior among different grading schemes but also provide fundamental data support for calculating the sintering activation energy using the Arrhenius equation, thereby revealing the mechanism of densification delay from an energetic perspective. The sintering activation energy can be calculated based on the Arrhenius equation using the Eqs. (1)–(3) [46,47]:

$$\ln\left(T\cdot\frac{\mathrm{d}L}{\mathrm{d}T}\cdot\frac{\mathrm{d}T}{\mathrm{d}t}\right)=-\frac{Q}{RT}+\ln k_0+\ln d^m+\ln f(L) \quad (1)$$

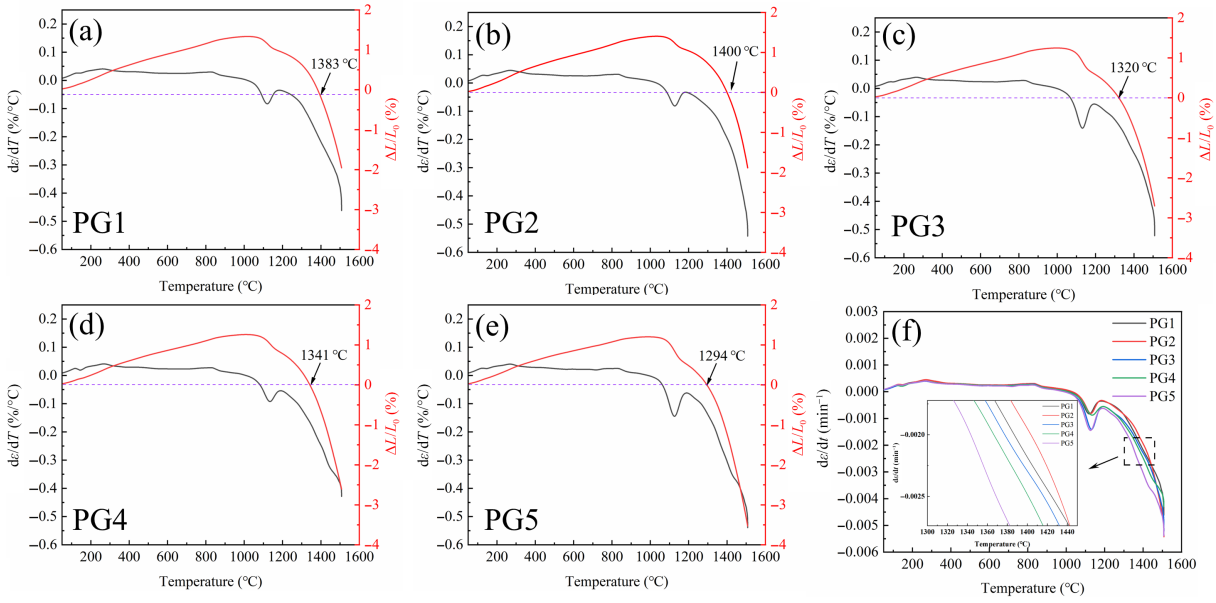

Fig. 10 Thermal expansion coefficients and strain of (a) PG1, (b) PG2, (c) PG3, (d) PG4, and (e) PG5. (f) Densification rate curves of PG1–PG5.

$$f(L) = \frac{L^{1-n}}{n} \tag{2}$$

$$k_0 = \frac{AD_0\Omega\gamma}{d^m} \tag{3}$$

where T is the temperature, L is the relative shrinkage, t is the time, dL/dT is the first derivative of strain with respect to temperature, and the heating rate (dT/dt) is kept constant at 18 °C/min, Q is the activation energy, R is the ideal gas constant (8.314 J/(mol·K)), d is the grain size, n, A, and m depend on the specific geometric model assumed for the particles, D_0 is the preexponential factor of the diffusion coefficient, Ω is the atomic volume, and γ is the surface free energy, respectively. Based on the above definitions, the terms involving grain size (d^m) and the prefactor (k_0) are considered constant C. It is imperative to clarify the experimental and theoretical boundaries justifying these approximations. Experimentally, the continuous shrinkage data were recorded via TMA exclusively during the nonisothermal heating phase up to 1550 °C, meaning that the analysis strictly captures the initial to early-intermediate stages of sintering. According to classical sintering theory, mass transport in this dynamic heating stage is predominantly driven by neck growth and pore elimination. Severe grain coarsening, which alters diffusion paths, typically occurs during the prolonged isothermal holding stage at peak temperatures (1600 °C in a muffle furnace). Therefore, the assumption of a near-constant grain size (d) within this specific, limited TMA evaluation window is physically well justified. Furthermore, since the maximum value of L within the selected fitting range is only 0.0353, the logarithmic variation of the function $f(L)$ is mathematically negligible compared to the dramatic change in the dominant exponential term driven by 1/T. Consequently, the term ln$f(L)$ remains essentially unchanged and can be safely approximated as a constant C without altering the slope of the Arrhenius plot, which solely dictates the activation energy (Q). Thus, Eq. (1) can be simplified and rearranged into Eq. (4) [48]:

$$\ln\left(T \cdot \frac{\mathrm{d}L}{\mathrm{d}T} \cdot \frac{\mathrm{d}T}{\mathrm{d}t}\right) = -\frac{Q}{RT} + C \tag{4}$$

The sintering activation energy (Q) was calculated using Eq. (4) based on the shrinkage data obtained from TMA tests. Specifically, the activation energy was derived from the slope of the Arrhenius plot of ln(T·dL/dT·dT/dt) versus 1/T. Figure 11 shows the linear fitting plots for each sample. Based on the slopes of the fitted lines, the calculated sintering activation energies for PG1–PG5 are 137.95, 244.68, 162.24, 132.61, and 129.95 kJ/mol, respectively. To validate the robustness of these calculations, the linear correlation coefficients (R^2) for all Arrhenius plots were determined to be greater than 0.98, confirming the high reliability of the selected fitting ranges and minimal experimental variability. Comparative analysis indicated that the powder grading strategy had a decisive influence on the sintering energy barrier. The quaternary particle grading PG5 sample exhibited the lowest sintering activation energy, implying that it required the lowest energy barrier for densification and possessed the most active mass transport. This low-energy barrier characteristic was attributed to the efficient packing and multilevel contact network of micro/nanoparticles in PG5, which effectively shortened the diffusion paths and provided a higher driving force for sintering [49–51]. In contrast, the binary grading PG2 sample showed an activation energy as high as 244.68 kJ/mol. This elevated value did not imply a shift in the fundamental diffusion mechanism but rather reflected the severe kinetic limitations inherent to its specific microstructural configuration. As a binary system comprising exclusively the two coarsest particle fractions, PG2 possessed the lowest specific surface area. The loose packing structure formed solely by coarse particles inevitably increased the effective mass transport distances between contact points, which necessitated a substantially higher initial thermal input to trigger the sintering process. This immense kinetic resistance made it difficult to initiate rapid densification under the same thermal conditions, which explained the delayed densification phenomenon. Furthermore, it was essential to clarify that the apparent activation energy and the macroscopic density evolution were governed by two distinct physical mechanisms: sintering kinetics and initial geometric packing, respectively. For instance, the calculated activation energy of binary PG1 was notably lower than that of ternary PG3. This kinetic advantage stemmed from the fact that PG1 contained a significantly higher fraction (25%) of UA2 than PG3 (15%). A higher proportion of fine particles effectively lowered the global energy barrier for atomic migration,

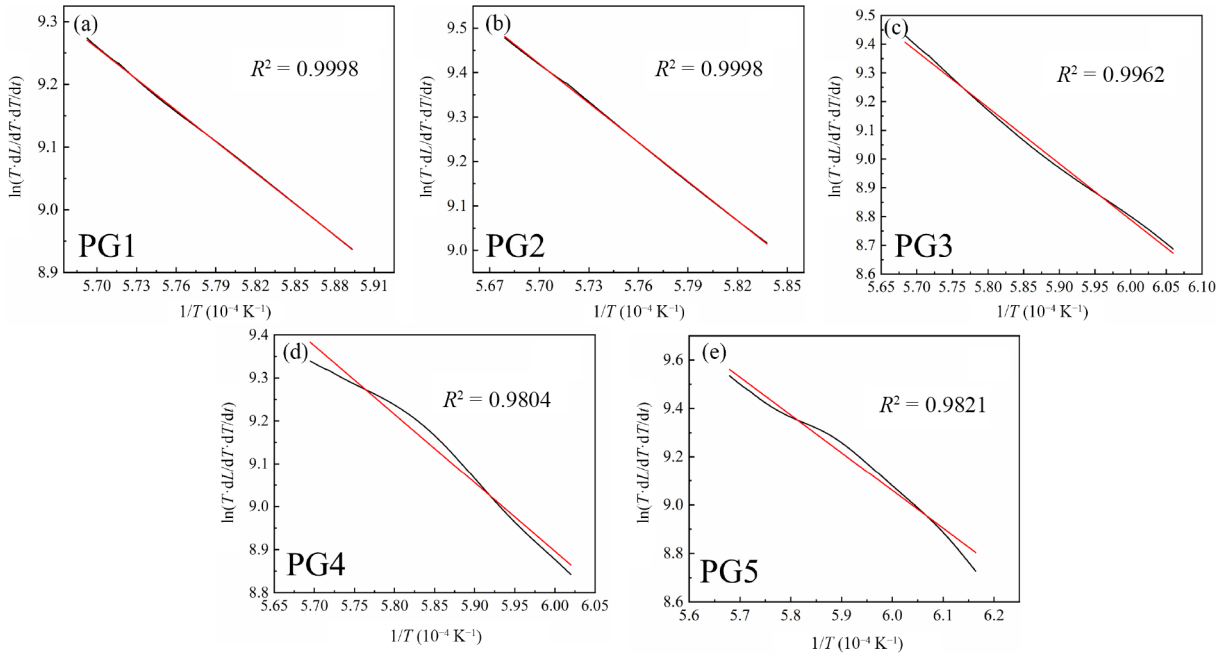

Fig. 11 ln(T·dL/dT·dT/dt) as a function of 1/T: (a) PG1, (b) PG2, (c) PG3, (d) PG4, and (e) PG5.

granting PG1 a faster intrinsic densification rate. However, from the perspective of geometric space occupation, the ternary PG3 system adhered more strictly to the hierarchical filling principles of the Horsfield model. Consequently, PG3 established a massive structural advantage during the green body forming stage, achieving a higher initial green density of 2.10 g/cm^3. During the prolonged sintering process, this inherent geometric superiority in initial spatial compactness heavily compensated for its slightly slower kinetics and ultimately dominated the macroscopic densification. Therefore, despite having a higher activation energy than PG1, PG3 consistently exhibited a higher density. A previous study reported that the sintering activation energy for conventional, coarse-grained Al_2O_3 typically ranges over 300 kJ/mol [48]. Therefore, the activation energy of PG2 aligned well with the expected theoretical regime for conventional coarse powders. Based on previous investigation, the sintering activation energy of single-sized UA4 was found to be 333.07 kJ/mol, whereas single-sized UA2 exhibited a significantly lower value of 106.15 kJ/mol [48]. This provided direct evidence that small, nonagglomerated particles inherently possessed much lower intrinsic sintering energy barriers. In stark contrast, the significantly lower activation energy of PG5 (129.95 kJ/mol) decisively demonstrated that the multiscale hierarchical inclusion of highly active nanoparticles effectively shortened diffusion pathways and overcame the massive energy barriers typical of conventional alumina sintering. In the quaternary PG5 system, 103 nm nanoparticles were precisely nested within the multilevel interstices of the micron-scale skeleton. These nanoscale nodes, characterized by extremely high surface curvature, generated massive local capillary driving forces and steep vacancy concentration gradients. More importantly, they constructed an exceptionally dense network of micro/nano grain boundary contacts. This unique geometric configuration drastically increased the density of grain boundary diffusion channels. The activation energy values further confirm that incorporating nanoscale fine particles and optimizing their spatial distribution are key mechanisms for lowering the sintering temperature and accelerating densification kinetics.

To further elucidate the fundamental origin of this sintering shrinkage phenomenon beyond the TMA, Rietveld refinement was performed on the XRD patterns of the sintered ceramics to track the densification process at the atomic level, as shown in Fig. 12. The refinement yielded highly reliable fits, with R_{wp} values ranging from 4.74% to 5.65% and χ^2 values below 1. The refined crystallographic parameters revealed a systematic lattice contraction that perfectly mirrored the macroscopic densification trends. The unit cell volume exhibited a monotonic decrease with the optimization of the particle grading: PG2 (255.1409 Å^3) > PG1 (255.0904 Å^3) > PG3 (255.0672 Å^3) > PG4 (255.0083 Å^3) > PG5 (254.9982 Å^3). This crystallographic evolution provided atomic-scale evidence for the multiscale grading mechanism. In the optimal quaternary PG5 system, the discretely distributed nanoparticles acted as highly active energetic nodes. During the high-temperature sintering stage, the extreme surface curvature of these nanoparticles generated a massive capillary stress. This intense compressive stress not only drove the rapid elimination of intergranular pores but also exerted a confining pressure on the α-Al_2O_3 lattice, inducing the observed intrinsic volume contraction. Therefore, the reduced apparent activation energy and the accelerated macroscopic densification kinetics were fundamentally rooted in this atomic-level lattice compaction, decisively proving the thermodynamic superiority of the quaternary monodisperse grading strategy.

To comprehensively elucidate the underlying mechanism responsible for the rapid densification and superior mechanical properties of PG5, Fig. 13 shows the schematic mechanism evolving from particle packing to microstructural evolution. The four types of spherical powders, characterized by uniform particle size and monodispersity, laid the foundation for constructing a highly ordered and dense structure. First, regarding geometric packing, the high uniformity, monodispersity, and sphericity of the raw powders eliminated interferences such as agglomeration, which are common in traditional irregular powders. In contrast to the binary particle grading (PG1 and PG2), where difficult-to-eliminate voids formed within the coarse particle skeleton, the monodispersed fine particles (UA1 and UA2) in the quaternary particle grading (PG5) acted as balls during the forming process. They flowed and rearranged efficiently, accurately embedding into

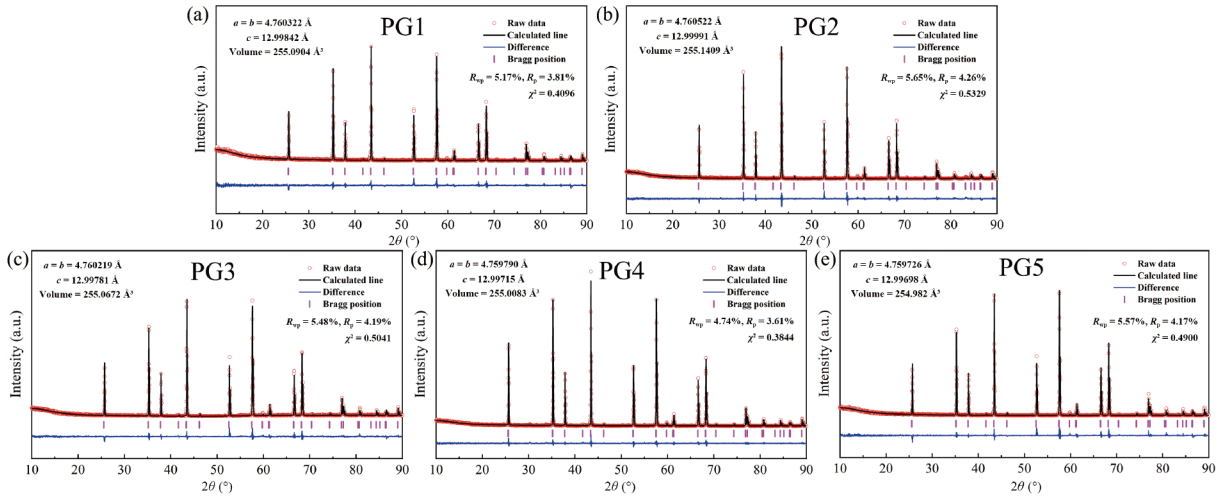

Fig. 12 Rietveld refinement results of five graded ceramics after sintering at 1600 °C for 6 h: (a) PG1, (b) PG2, (c) PG3, (d) PG4, and (e) PG5.

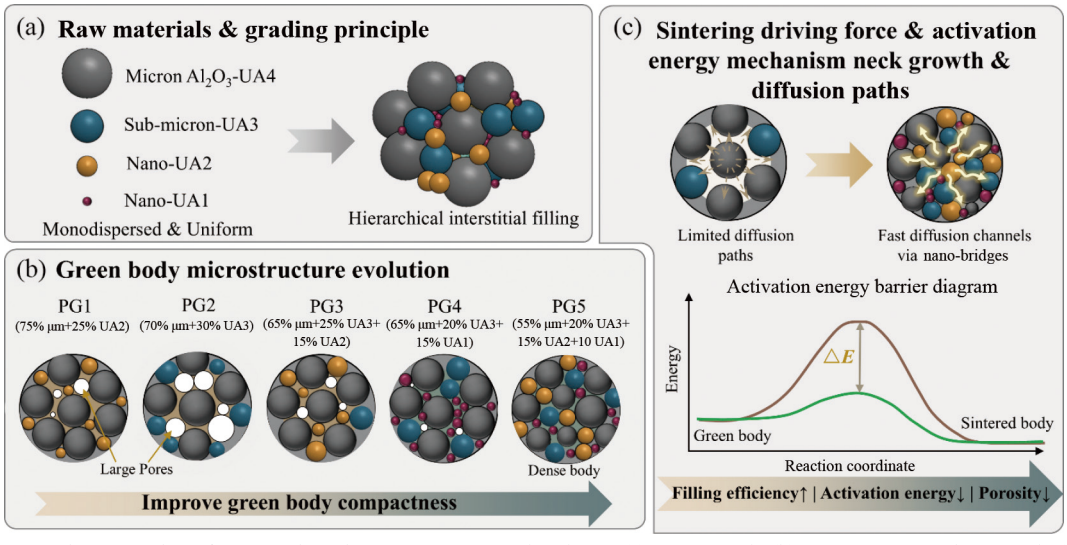

Fig. 13 Schematic mechanism evolving from particle packing to microstructural evolution: (a) raw materials, (b) microstructure evolution, and (c) mechanism of changes in sintering activation energy.

the interstices formed by larger particles with ideal geometry. This hierarchical filling effect, based on monodispersed particles, significantly enhanced the initial packing density, as shown in Figs. 13(a) and 13(b). Second, this could be explained from a kinetic perspective: particle size uniformity ensured the consistency of the sintering driving force. It was imperative to clarify that the uniformity here referred to the strict monodispersity within each powder (UA1–UA4). This uniformity ensured that the localized sintering driving force provided by these fine particles was highly consistent throughout the entire macroscopic bulk. The introduced monodispersed nanoparticles possessed extremely high and uniform sintering activity, acting as initiators for densification in the early stage. This avoided differential sintering or abnormal grain growth often caused by a broad particle size distribution. These nanoparticles preferentially induced synchronized neck formation at the contact points of micron-sized particles, driving rapid mass diffusion via consistent high capillary forces. The highly curved surfaces of the incorporated monodisperse nanoparticles generated massive local capillary stresses. According to classical sintering theory, this amplified capillary driving force significantly increased the vacancy concentration gradient between the pore surfaces (vacancy sources) and the grain boundaries (vacancy sinks), thereby accelerating atomic flux. The hierarchical interstitial filling inherently refined the local microstructural network, drastically increasing the total grain boundary area per unit volume. This massively expanded boundary network acted as a dense array of "fast-track" mass transport channels. The dominant mass transport mechanism was effectively shifted toward lower-energy grain boundary diffusion. Therefore, the combination of amplified capillary driving forces, multiplied grain boundary diffusion pathways, and absolutely shortened diffusion distances collectively reduced the macroscopic energy barrier required for global atomic migration. This synergistic effect significantly reduced the energy barrier required for atomic migration—namely, the sintering activation energy—thereby overcoming the densification delay and achieving uniform shrinkage during the sintering process, as shown in Fig. 13(c). Finally, benefiting from the monodispersity of the raw materials, PG5 ultimately evolved into a dense microstructure with a uniform grain size distribution and no coarse grains. The strongly bonded grain boundaries effectively eliminated micro/nanopores that typically served as stress concentration sources. Under external loading, the dense grain interlocking structure substantially dissipated fracture energy, thereby endowing the ceramic with excellent mechanical properties. In summary, the quaternary multiscale particle grading

strategy relied on the uniformity of the particle size and reaction activity of the monodispersed powders. Through the dual mechanisms of geometric filling and the reduction of sintering activation energy, the perfect reconstruction of the Al_2O_3 ceramic microstructure and a significant enhancement in mechanical properties were achieved.

4 Conclusions

In this study, particle grading ranging from binary to quaternary was constructed using four types of monodispersed, spherical α-Al_2O_3 powders with uniform particle sizes. By utilizing the dual mechanisms of optimizing powder geometric packing and reducing the sintering energy barrier, rapid densification and enhanced mechanical properties of the ceramics were achieved. The main conclusions are as follows: (1) Benefiting from the high monodispersity of the raw powders, the grading of the quaternary particles (PG5) utilized nanoscale fine powders to hierarchically fill the interstices within the micron-sized skeleton. Compared with the binary (PG1 and PG2) and ternary (PG3 and PG4) grading systems, PG5 achieved the lowest porosity (0.1%) and the highest bulk density (3.84 g/cm^3) after sintering at 1600 °C. SEM and FIB–TEM results demonstrated tightly bonded grains and clean grain boundaries free of nanoscale pores. Furthermore, Micro–CT 3D reconstruction proved the absence of macroscopic voids and interconnected pore networks, thereby validating the integrity and uniformity of the microstructure from a multiscale perspective. (2) The particle grading directly determines the energy barrier of the sintering process. The apparent sintering activation energy of quaternary PG5 decreased to a minimum (129.95 kJ/mol), which was significantly lower than that of binary PG2 (244.68 kJ/mol). The results of the Rietveld refinement also showed the same trend. This result revealed the essence: introducing high-activity nanoscale monodispersed components to construct a multilevel contact network effectively lowered the energy barriers by drastically amplifying the capillary driving forces and providing a massive density of fast-track grain boundary diffusion pathways. Consequently, this overcame the densification delay observed in binary systems and provided the core thermodynamic driving force for low-temperature RS. (3) Synergistic enhancement of mechanical properties. Relying on the coupling effect of geometric packing and sintering activation energy, the mechanical properties of the ceramics exhibited a significant upward trend with the diversification of particle grading (quaternary > ternary > binary). PG5 initiated sintering at a lower temperature and completed densification rapidly. This ultimately led to the reconstruction of the microstructure and a comprehensive improvement in performance. PG5 exhibited superior comprehensive properties, with the Vickers hardness, flexural strength, and elastic modulus reaching peaks of 18.5 GPa, 278.9 MPa, and 355.5 GPa, respectively.

Acknowledgements

The authors acknowledge the financial support by the National Natural Science Foundation of China (Grant No. 52472232).

Availability of data and materials

The data that support the findings of this study are available from the corresponding author upon reasonable request.

Competing interests

The authors have no competing interests to declare that are relevant to the content of this article.

References

[1] Yang H, Li Y, Huang Y, *et al.* Revisiting 1 GPa alumina ceramics. *J Adv Ceram* 2025, **14**: 9221184.

[2] Liu Y, Yin H, Tang Y, *et al.* Phase evolution and lightweight application of dolomite@Al_2O_3 spherical particle with core–shell structure. *J Am Ceram Soc* 2023, **106**: 1458–1472.

[3] Gu Q, Sun L, Ji X, *et al.* High-performance and high-precision Al_2O_3 architectures enabled by high-solid-loading, graphene-containing slurries for top-down DLP 3D printing. *J Eur Ceram Soc* 2023, **43**: 130–142.

[4] Paydar MH, Ganji pour A. Comparative study of dry pressing, isostatic pressing, and gel casting for fabricating porous alumina ceramics. *J Mater Res Technol* 2026, **40**: 2805–2819.

[5] Wang J, Lu D, Xuan W, *et al.* Boron nitride microribbons strengthened and toughened alumina composite ceramics with excellent mechanical, dielectric, and thermal conductivity properties. *J Adv Ceram* 2024, **13**: 496–506.

[6] Xiong Z, Zhang K, Liao W, *et al. In situ* synthesis of high-entropy Al_2O_3/$RE_3Al_5O_{12}$/ZrO_2 ceramic by laser powder bed fusion with exceptional properties. *J Adv Ceram* 2024, **13**: 2004–2020.

[7] Zhang Z, Li Y, Li Y, *et al.* Effect of alumina content on the exsolution behavior and crystal structure of magnesia alumina spinel. *J Eur Ceram Soc* 2026, **46**: 118160.

[8] Kang Y, Yang H, Wei Y, *et al.* Achieving near-theoretical transparency in alumina ceramics by refining nanograins. *Adv Opt Mater* 2026, **14**: 02109.

[9] Xing H, Jiang W, Wang X, *et al.* Preparation and precision control of alumina-based ceramic core using the SLA-Micromilling hybrid process. *Addit Manuf* 2026, **118**: 105095.

[10] Biesuz M, Abate WD, Sglavo VM. Porcelain stoneware consolidation by flash sintering. *J Am Ceram Soc* 2018, **101**: 71–81.

[11] Biesuz M, Sglavo VM. Flash sintering of ceramics. *J Eur Ceram Soc* 2019, **39**: 115–143.

[12] Fang H, Zhou B, Huang P, *et al.* Rapid fabrication of high-density YAG ceramics via spark plasma sintering of mesoporous YAG powder. *J Am Ceram Soc* 2026, **109**: 70527.

[13] Smith DS, Martinez Dosal J, Oummadi S, *et al.* Neck formation and role of particle-particle contact area in the thermal conductivity of green and partially sintered alumina ceramics. *J Eur Ceram Soc* 2022, **42**: 1618–1625.

[14] Wang X, Zhang L, Ji Y, *et al.* $Gd_2Zr_2O_7$ ceramics synthesized by solid-state reactive sintering: Effects of starting powders with different-scale particle sizes. *Ceram Int* 2022, **48**: 16839–16844.

[15] Chen B, Yuan L, Zhang Z, *et al.* Effect of sintering path and initial particle size on pressure-less sintering behaviour and kinetics of non-equiaxed nano-alumina. *Ceram Int* 2025, **51**: 19552–19561.

[16] Palmeira AA, Bondioli MJ, Strecker K, *et al.* Densification and grain growth of nano- and micro-sized Y-TZP powders. *Ceram Int* 2016, **42**: 2662–2669.

[17] Aminzare M, Mazaheri M, Golestani-fard F, *et al.* Sintering behavior of nano alumina powder shaped by pressure filtration. *Ceram Int* 2011, **37**: 9–14.

[18] Liang Z, Zhang H, Li Y, *et al.* A reverse particle grading strategy for design and fabrication of porous SiC ceramic supports with improved strength. *J Adv Ceram* 2024, **13**: 1011–1022.

[19] Li X, Li J, Niu S, *et al.* Regulation of anisotropy in vat photopolymerization of silica-based ceramic cores based on particle grading. *Ceram Int* 2025, **51**: 52768–52776.

[20] Li X, Su H, Dong D, *et al.* Enhanced comprehensive properties of stereolithography 3D printed alumina ceramic cores with high porosities by a powder gradation design. *J Mater Sci Technol* 2022, **131**: 264–275.

[21] Liu K, Sun Y, Sun H, *et al.* Effect of particle grading on the properties of photosensitive slurry and $BaTiO_3$ piezoelectric ceramic via digital light processing 3D printing. *J Eur Ceram Soc* 2023, **43**: 3266–3274.

[22] Xiao C, Zheng H, Li X. Improving the properties and high temperature oxidation resistance of polycrystalline cubic BN composites through regulating particle size and adding SiC whiskers. *Ceram Int* 2025, **51**: 48549–48557.
[23] Qian C, Hu K, Wang H, *et al.* The effect of particle size distribution on the microstructure and properties of Al_2O_3 ceramics formed by stereolithography. *Ceram Int* 2022, **48**: 21600–21609.
[24] Shi ZA, Wu JM, Fang ZQ, *et al.* Particle surface oxidation modification and particle gradation strategy for the preparation of high-strength SiC ceramics via vat photopolymerization. *Addit Manuf* 2024, **84**: 104118.
[25] Yin S, Sun C, Li X, *et al.* Phase composition, microstructure, and mechanical properties of ZTA ceramics prepared by gelcasting using multi-gradation spherical powders. *J Alloys Compd* 2025, **1017**: 178984.
[26] Zhu M, Xia Y, Yao D, *et al.* Effects of particle gradation and Gd_2O_3 content on the properties of porous Al_2O_3 ceramics. *Ceram Int* 2025, **51**: 35711–35717.
[27] Liu X, Yuan Y, Wang R, *et al.* Pressureless sintering behaviour of Al_2O_3/ZrO_2 amorphous/solid solution powder with ultra-fine ZrO_2 nanoparticle precipitation. *Ceram Int* 2023, **49**: 39886–39897.
[28] Wang Z, Mai Z, Wu Y, *et al.* Preparation of spherical α-Al_2O_3 nanoparticles by microwave hydrothermal synthesis and addition of nano-Al seeds. *J Am Ceram Soc* 2022, **105**: 5585–5597.
[29] Wang J, Raj R. Activation energy for the sintering of two-phase alumina/zirconia ceramics. *J Am Ceram Soc* 1991, **74**: 1959–1963.
[30] Drdlik D, Sokolov I, Hadraba H, *et al.* Sintering activation energies of anisotropic layered and particle alumina/zirconia-based composites and their mechanical response. *Ceram Int* 2024, **50**: 37430–37440.
[31] Stanfield AD, Smith SM, Filipović S, *et al.* Final-stage densification kinetics of direct current–sintered ZrB_2. *J Am Ceram Soc* 2023, **106**: 5654–5661.
[32] Xu F, Zhang H, Xie F, *et al.* Investigation of grain boundary diffusion and grain growth of lithium zinc ferrites with low activation energy. *J Am Ceram Soc* 2018, **101**: 5037–5045.
[33] Huo M, Ren J, Zhang J, *et al.* Surface reconstruction and performance regulation of Al_2O_3 powder: Key mechanisms of calcination atmosphere. *Ceram Int* 2025, **51**: 56498–56507.
[34] Huo M, Ren J, Zhang J, *et al.* Morphology retention and phase transformation mechanisms of Al_2O_3 powders under atmosphere-controlled calcination. *Ceram Int* 2025, **51**: 48063–48074.
[35] Huo M, Ren J, Zhang J, *et al.* Hydrothermal synthesis and phase transformation evolution of monodisperse spherical α-Al_2O_3 powders with uniform particle size for advanced ceramic applications. *Ceram Int* 2025, **51**: 40822–40832.
[36] Huo M, Qu H, Zhang J, *et al.* Coupled multivariable synthesis of uniform, monodisperse, and multi-scale spherical precursors and α-Al_2O_3 powders. *J Am Ceram Soc* 2026, **109**: 70576.
[37] Li Q, An X, Liang J, *et al.* Balancing flexural strength and porosity in DLP-3D printing Al_2O_3 cores for hollow turbine blades. *J Mater Sci Technol* 2022, **104**: 19–32.
[38] Batistão BF, de Traglia Amancio-Filho S, da Silva LVM, *et al.* Tailoring ceramic particle size and fraction to optimize aluminum powders for additive manufacturing. *J Mater Res Technol* 2026, **41**: 2500–2517.
[39] Li W, Gan R, You J, *et al.* Porous alumina ceramics with integrated open and closed pores synthesized from thermal-oxidation of colloidal assembled aluminum particles via freeze casting. *J Eur Ceram Soc* 2026, **46**: 118146.
[40] Chen Z, Chen P, Zhao S, *et al.* Porous Al_2O_3–$MgAl_2O_4$ foam ceramics with ultra-high porosity and secondary pores via particle-stabilized foaming method. *J Am Ceram Soc* 2026, **109**: 70519.
[41] Li X, Reza-E-Rabby M, Guzman A, *et al.* Strain and strain rate in friction extrusion. *J Mater Res Technol* 2022, **20**: 882–893.
[42] Kultayeva S, Kim YW, Song IH. Influence of sintering atmosphere and BN additives on microstructure and properties of porous SiC ceramics. *J Eur Ceram Soc* 2021, **41**: 6925–6933.
[43] Miao K, Liu L, Cao J, *et al.* Zero sintering-induced shrinkage of porous oxide ceramics. *J Mater Sci Technol* 2023, **159**: 184–193.
[44] Li F, Luo H, Cao L, *et al.* Sintering densification driven by orientation fluctuation in textured $BaTiO_3$ ceramics with abnormal comprehensive ferroelectric properties. *J Adv Ceram* 2025, **14**: 9221126.
[45] Wang H, Li X, Xu X, *et al.* MgF_2-based microwave dielectric ceramics with ultra-low sintering temperature and high thermal expansion coefficient. *J Eur Ceram Soc* 2024, **44**: 2150–2156.
[46] Ye CC, Wei WQ, Fu X, *et al.* Effect of sintering activation energy on Si_3N_4 composite ceramics. *Ceram Int* 2022, **48**: 4851–4857.
[47] Dehaudt P, Bourgeois L, Chevrel H. Activation energy of UO_2 and UO_{2+x} sintering. *J Nucl Mater* 2001, **299**: 250–259.
[48] Huo M, Ren J, Zhang J, *et al.* Study on the structure-performance relationship of sintering kinetics and mechanical properties in monodisperse spherical α-Al_2O_3 powders regulated by particle size gradient. *J Eur Ceram Soc* 2026, **46**: 117969.
[49] Jin WL, Zhou SJ, Li JH, *et al.* Synergistic enhancement on mechanical and cutting performances of Ti(C,N)-based cermets by tailoring raw WC particle size. *Ceram Int* 2025, **51**: 39099–39109.
[50] Guan D, Wang X, Chen X, *et al.* Powder grading for enhanced properties in DLP 3D printed silica ceramic cores. *J Alloys Compd* 2026, **1050**: 185807.
[51] Yang H, Liu W, Chen S, *et al.* On the two-step sintering of fine-grained alumina ceramics using gel-casted Sumitomo powders. *J Am Ceram Soc* 2026, **109**: 70289.